Gaining control of lipid-based nanomedicine by understanding the nano-bio interface
Pattipeiluhu, R.

Chapter 5

Paracrystalline Inverted Lipid Phases Encapsulating siRNA Enhance Lipid Nanoparticle Mediated Transfection

Efficient cytosolic delivery of RNA molecules remains a formidable barrier for RNA therapeutic strategies. Lipid nanoparticles (LNPs) serve as state-of-the-art carriers that can deliver RNA molecules intracellularly, as exemplified by the recent implementation of several vaccines against SARS-CoV-2. Using a bottom-up rational design approach, we assemble LNPs that contain programmable lipid phases encapsulating small interfering RNA (siRNA). A combination of cryogenic transmission electron microscopy, cryogenic electron tomography and small-angle X-ray scattering reveals that we can form inverse hexagonal structures, which are present in a paracrystalline nature within the LNP core. Comparison with lamellar LNPs reveals that the presence of inverse hexagonal phases enhances the intracellular silencing efficiency over lamellar structures. We then demonstrate that lamellar LNPs exhibit an *in situ* transition from a lamellar to inverse hexagonal phase upon interaction with anionic membranes, whereas LNPs containing pre-programmed paracrystalline hexagonal phases bypass this transition for a more efficient one-step delivery mechanism, explaining the increased silencing effect. This rational design of LNPs with defined lipid structures aids in the understanding of the nano-bio interface and adds substantial value for new avenues of LNP design, optimization and use.

5.1 Introduction

RNA therapy relies on delivery of exogenous (therapeutic) RNA molecules, such as messenger (mRNA) or small interfering RNA (siRNA), to control disease-relevant gene expression.[1–3] For efficient functional cytosolic delivery to, and release within, target cells, these highly charged, immunogenic and membrane-impermeable RNA molecules require the use of delivery systems.[4–6] To this end, ionizable lipid nanoparticles (LNPs) serve as state-of-the-art vehicles that can package, protect and release RNA molecules inside cells.[7,8] LNPs have realized the translation of RNA therapeutics to the clinic, highlighted by the approval of Onpattro®,[9] enabling RNA interference (RNAi) therapy for the treatment of polyneuropathies resulting from transthyretin-mediated amyloidosis.[10] In addition, this platform has been successfully expanded for the delivery of other RNA molecules, yielding safe and effective mRNA-based vaccines for SARS-CoV-2.[11,12]

LNPs are multicomponent systems typically composed of an ionizable cationic lipid (IL), phospholipid, cholesterol, PEG-lipid and an nucleic acid payload, formulated through rapid microfluidic mixing.[13,14] At a pH below its pKa, the ionizable lipids enable electrostatic complexation of anionic nucleic acid molecules, followed by self-assembly and buffer exchange to physiological pH to form nanostructures with a core-shell structure in the range of ~30-150 nm.[15] The LNP core is considered "hydrophobic", being rich in ionizable lipids, cholesterol and its nucleic acid payload, in contrast, the LNP surface (*i.e.* lipid-water interface) is rich in helper phospholipids and lipid-PEG conjugates.[16] Intracellular unpacking and delivery to the cytosol of the encapsulated RNA molecules relies on endosomal acidification and *in situ* protonation of the ILs, leading to an electrostatic interaction with the endosomal membrane.[17] Disruption of the LNP structure and endosomal membrane is crucial for sufficient cytosolic RNA delivery.[18,19] However, in this process the majority (≥98%) of RNA molecules delivered with LNP systems remain trapped inside endosomal and lysosomal compartments, leading to degradation or efflux out of the cell.[20,21] To this end, empirical studies exploring the chemical space of LNP components, for example the diversification of IL structures,[22–27] or the variation of helper and PEG-lipids,[28–32] has been pursued in order to improve LNP mediated transfection efficiency. More recently, similar studies have been coupled with biophysical characterization of lipid structures in LNPs, aiming to understand the importance of LNP lipid organization and structure on their biological activity.[33,34] However, characterization and identification of defined lipid structures in LNPs, and the mechanistic understanding of these how structures affect LNP-endosome interaction and RNA delivery into the cytoplasm, remains

elusive. Nevertheless, a fundamental understanding of these mechanisms can aid the development of more potent LNP nanomedicines.

Here, we present bottom-up rational design of LNPs with defined lipid superstructures encapsulating siRNA, in order to accurately study their structure-activity relationship. Using cryogenic transmission electron microscopy (cryoTEM), cryogenic electron tomography (cryoET) and small angle X-ray scattering (SAXS), we identify and characterize defined lamellar, paracrystalline inverted hexagonal or mixed lipid-RNA structures in the core of LNPs, and are able to successfully differentiate between empty lipid structures and those containing siRNA. By combining cryoTEM and SAXS, we gain insights into the thermal stability of these structures and demonstrate that thermally-stable paracrystalline inverse hexagonal lipid phases encapsulating siRNA enhance the LNP-mediated transfection efficiency over lamellar variants. Our data supports the notion that lamellar LNP formulations induce an *in situ* transition from a lamellar to inverse hexagonal phase upon interaction with anionic membranes, whereas LNPs with pre-programmed inverse hexagonal phases can bypass this transition for a more efficient one-step delivery mechanism. We believe that our rational approach and biophysical characterization will yield new avenues for LNP design and development and can improve the efficiency of RNA therapeutics.

5.2 Results

The formation of lipid superstructures is dictated by the composition and ratio of different lipids with distinctive biophysical properties, such as transition temperature, charge, hydrophobicity and intrinsic curvature.[35] This is utilized in the field of nanomedicine in order to generate non-lamellar and crystalline lipid nanoparticles.[36,37] For example, the formation of inverted lipid structures is dependent on an abundance of lipids that possess a intrinsic negative ($R_0 < 0$) curvature, such as the lipid 1,2-dioleoyl-sn-glycero-3-phosphoethanolamine (DOPE) (**Figure 1a**).[38] Here, we aimed to rationally design LNP systems containing lamellar or inverted structures encapsulating siRNA in order to assess their biophysical properties and structure-activity relationship. We envisioned that generation of lamellar or inverted phases in the core of LNPs could be achieved by manipulation of the DOPE lipid content (mol%), substituting for cholesterol (**Figure 1b,c**). We chose three different formulations, in which the molar ratios of the model ionizable lipid (IL) 1,2-dioleoyl-3-dimethylammonium-propane (DODAP) and PEG lipid 1,2-dimyristoyl-sn-glycero-3-phosphoethanolamine-N-methoxypolyethylene glycol-2000 (DMPE-PEG2000) were kept constant, while varying in DOPE content at 10, 30 and 49 mol% (**Figure 1c, Figure S1**). These formulations are referred to as 10PE-LNP, 30PE-LNP

and 49PE-LNP respectively. The small interfering RNA (siRNA) molecule Patisiran®,[10] used in the clinically approved LNP formulation Onpattro®,[9] was chosen a model oligonucleotide cargo (**Table S1**). Duplexed siRNA molecules for therapeutic purposes are short (~18-22 base pairs),[39] display high structural similarity and are less prone to structural deformation or the formation of secondary structures compared to mRNA,[40] which aids in the formation of predictable and reproducible lipid-RNA structures. LNP formulations were assembled with different ionizable lipid (nitrogen, N) to siRNA ratios (phosphate, P) ratios, being: no RNA, NP = 6 and NP = 1 (noted as 10PE-LNP-noRNA, 10PE-LNP-NP6 or 10PE-LNP-NP1, *etc.*). A NP ratio of 6 is commonly applied for oligonucleotide payloads such as siRNA or mRNA in order to achieve a sufficient encapsulated dose with high encapsulation efficiency,[41] whereas a NP ratio of 1 is known to have surpassed the maximum encapsulation capacity of RNA molecules in LNPs.[42] We performed a comparative analysis of these LNPs in order to determine the independent effects of RNA content and lipid composition on the formation of lipid-RNA superstructures. Conventional microfluidic mixing procedures were used to fabricate the LNPs (**Figure S2**). After dialysis, the hydrodynamic radius and surface charge of the LNPs were determined by dynamic light scattering (DLS) and zeta potential measurements, respectively (**Table S2**). Formulations with an NP ratio of 6 or 1 showed the formation of 100-150 nm particles with a polydispersity index (PDI) < 0.120, in which particle size slightly increased concomitantly with DOPE content. Assembly of 30PE-LNP-noRNA and 49PE-LNP-noRNA showed formation of larger and more polydisperse particles. In all cases, the surface charge varied between -1 to -5 mV, indicating the formation of zwitterionic neutral LNPs in PBS buffer, reflecting the expected formal charge of the lipid combination at physiological pH.

In order to gain insights into the formation of lipid structures in these formulations, we combined SAXS as bulk method with cryoTEM imaging to assess the difference in nanoscale structures of the assembled LNPs. All 10PE-LNP SAXS profiles displayed a Bragg reflection at a scattering vector $q \sim 0.1$ Å^{-1}, which was most pronounced at NP1. This is a hallmark of the formation of a defined structure for all NP ratios and its amplification by an increase in siRNA content in the assembly (**Figure 1d**). The associated cryoTEM revealed the formation of lamellar structures in all three formulations, in which 10PE-LNP-NP1 formed concentric circles extending to the LNP core (Black arrows, **Figure 1g, Figure S3a**). For 10PE-LNP-NP6 and 10PE-LNP-noRNA, structure formation was limited to several lamellar rings on the periphery, surrounding an amorphous core (**Figure S4**). When dialysis was performed with a molecular weight cut-off (MWCO) below the size of the siRNA (MWCO = 10 kDa) to exchange buffer but retain free RNA for effective encapsulation efficiency (EE%) determination, an EE% of roughly 50% indicated successful

saturation of encapsulation of 10PE-LNPs at a NP ratio of 1 (**Figure S5a**). Our data showing the amplification of lamellar structures and saturation of encapsulation are in line with previously reported LNPs with comparable lipid compositions and NP ratios.[15,42]

When the DOPE content was increased to 30 mol% (30PE-LNP variants), the Bragg reflection shifted towards smaller **q** values, indicating transition away from lamellar structures (**Figure 1e**). Two maxima around $q \sim 0.1$ Å⁻¹ are distinguishable for 30PE-LNP-noRNA and 30PE-LNP-NP6, whereas 30PE-LNP-NP1 showed a broad shoulder instead, suggesting that multiple structures may coexist. For 30PE-LNP-NP1, cryoTEM revealed the formation of various repeating and distinguishable structures. Similar to 10PE-LNP-NP1, lamellar structures could be identified (Black arrows, **Figure 1h, Figure S3b**) but, in addition, also non-lamellar structures were observed (White arrows, **Figure 1h**). In the case of 30PE-LNP-NP6 and 30PE-LNP-noRNA, similar lamellar and non-lamellar structures were observed (**Figure S6**). However, following the trend of the 10PE-LNP variants, these structures were less defined and the lamellar rings showed a lower signal amplification in the presence of siRNA compared to those observed in 30PE-LNP-NP1.

When the DOPE content was increased further to 49 mol% (49PE-LNP variants), the **q** ~ 0.1 Å⁻¹ reflection again shifted to lower **q** values (**Figure 1f**). In this case, both 49PE-LNP-NP1 and 49PE-LNP-noRNA showed discernable Bragg reflections. These occurred at lower *q* values for 49PE-LNP-NP1 than for 49PE-LNP-noRNA, indicating a difference in structure and/or domain size. The LNP-49PE-NP6 profile displays the principal reflections of both 49PE-LNP-NP1 and 49PE-LNP-noRNA, albeit less pronounced, indicating the formation of a mixture of the corresponding structures. In all of the LNP-49PE variants, cryoTEM revealed the sole formation of non-lamellar like structures (**Figure 1i, Figures S3c and S7**). Similar to 10PE-LNP-NP1, the 30PE-LNP-NP1 and 49PE-LNP-NP1 formulations displayed saturation of encapsulation, indicated by an EE% of roughly 50% (**Figure S5**). For all formulations, the large excess of siRNA could be removed by dialysis with a MWCO larger than free siRNA of 1 MDa, in order to avoid interference of unencapsulated siRNA in further experiments.
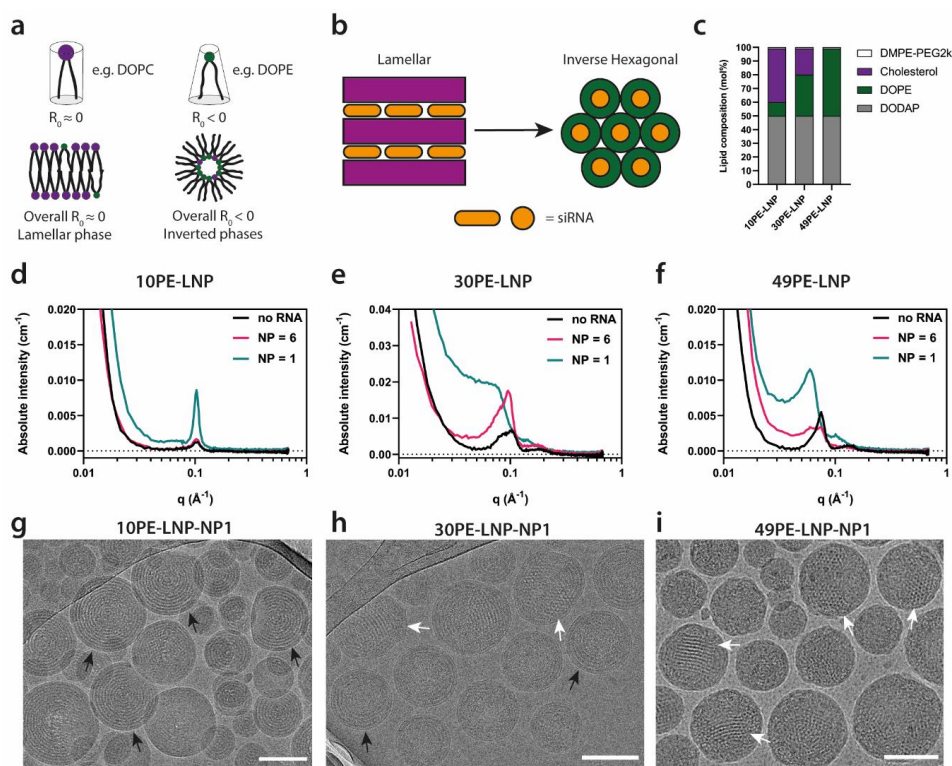
Figure 1. Design of LNPs containing defined lipid phases. (**a**) Curvature in lipid mixtures is driven by the composition of lipids with various curvature profiles Compositions with larger amounts of lipids with a $R_0 < 0$ lead to the formation of inverted phases. (**b**) Lamellar structures can transition towards inverted phases by the increase of DOPE lipid content. (**c**) LNP compositions designed to form lamellar and inverted lipid structures encapsulating siRNA used in this study. (**d**-**f**) SAXS profiles of the LNP compositions shown in c, at different NP ratios. (**g**-**i**) Representative cryoTEM images of the LNPs compositions in c, at NP ratio = 1. Scale bars are 100 nm.

Since 10PE-LNP, 30PE-LNP and 49PE-LNP assembled with an NP ratio of 1 formed particles of similar sizes, along with clearly defined lipid structures, they were subjected to comparative and in-depth structural analysis. For each of the formulations, a large number of single particles (n > 75) showing clear structural properties were selected from cryoTEM images and categorized based on structural similarity. The regions of interest were subjected to a fast Fourier transform (FFT), yielding the reciprocal lattice from which the repeating distance of a structure could be determined. In the case of 10PE-LNP-NP1, only lamellar concentric rings were observed throughout the sample. These structures displayed clear diffraction, as well as higher-order maxima, of the reciprocal space repeating unit,

specifically at 6.38 nm, 3.19 nm and 2.08 nm (**Figure 2a**). The initial scattering vector at 6.38 nm represents the lattice spacing of the primitive cell. Analyzing all of the selected single particles allowed us to construct a violin plot, revealing the variation in lamellar lattice spacing (**Figure 2b**). The mean lattice spacing of the lamellar structure is 5.88 nm ± 0.65 nm (n = 84). The large deviation in observed lattice spacings, which range from 4.20 nm to 6.90 nm, is not well reflected in the SAXS profile of 10PE-LNP-NP1, which displays a narrow peak at $q \sim$ 0.1 Å^{-1} (**Figure 1d**). In contrast to bulk SAXS measurements, cryoTEM imaging displays the structures within individual LNPs, which can present multiple orientations along the imaging axis. Consequently, this deviation in lattice spacings can be explained by an out-of-plane rotation of the lamellae to the electron beam, in which rotated lattices appear narrower (**Figure 2c**). Nevertheless, a preferential orientation for the lamellar spacing in vitreous water is observed and reflected by the median of 6.18 nm. This value closely reflects the expected values of lamellar lipid bilayers containing (phospho)lipids with similar carbon tail lengths (C$_{18}$) and cholesterol complexing oligonucleotides.[43,44]

For 30PE-LNP-NP1 samples, we identified three distinguishable and repetitive structures: hexagons, straight lines and lamellae (**Figure 2d**). Lattice spacing analysis of the individual structures in 30PE-LNP-NP1 revealed a high similarity for the straight lines and hexagons, at 5.78 nm ± 0.14 nm and 5.77 nm ± 0.14 nm respectively (**Figure 2e**). These values are slightly smaller than the mean lattice spacings of a = 6.26 nm ± 0.18 nm observed for 10PE-LNP-NP1. Interestingly, LNPs with a hexagonal and lamellar structure were found to co-exist, and in some cases, these structures were visualized within the same particle (**Figure S8**). This coexistence of LNPs with different structures and LNPs displaying coexisting structures within the same particle yields a broad scattering signal in the 30PE-LNP-NP1 SAXS profile instead of well-defined, distinguishable Bragg reflections (**Figure 1e**). For 49PE-LNP-NP1, hexagonal and straight-line structures similar to 30PE-LNP-NP1 were observed (**Figure 2f**). However, the presence of concentric lamellar structures was no longer observed. This absence of lamellar structures can be attributed to our rational design, given the high amount of DOPE lipids that possess a negative intrinsic curvature in the 49PE-LNP formulations. Quantification of the structures in 49PE-LNP-NP1 also yielded a high similarity in lattice spacing for straight lines and hexagons, at 6.10 nm ± 0.13 nm and 6.03 nm ± 0.12 nm respectively. This is in line with the presence of a very pronounced Bragg peak in the 49PE-LNP-NP1 SAXS pattern. Altogether, the observation of straight lines and hexagonal structures in 30PE-LNP-NP1 and 49PE-LNP-NP1 clearly indicates the presence of an inverse hexagonal tubular structure, imaged from different viewpoints by cryoTEM (**Figure 2h**). The expansion of the lattice of the inverted hexagonal

phase from a = 5.78 nm ± 0.14 nm for 30PE-LNP-NP1 to a = 6.06 nm ± 0.13 nm for 49PE-LNP-NP1, can be explained by the increase in C_{18}-tailed DOPE and concomitant reduction in cholesterol content.[45]
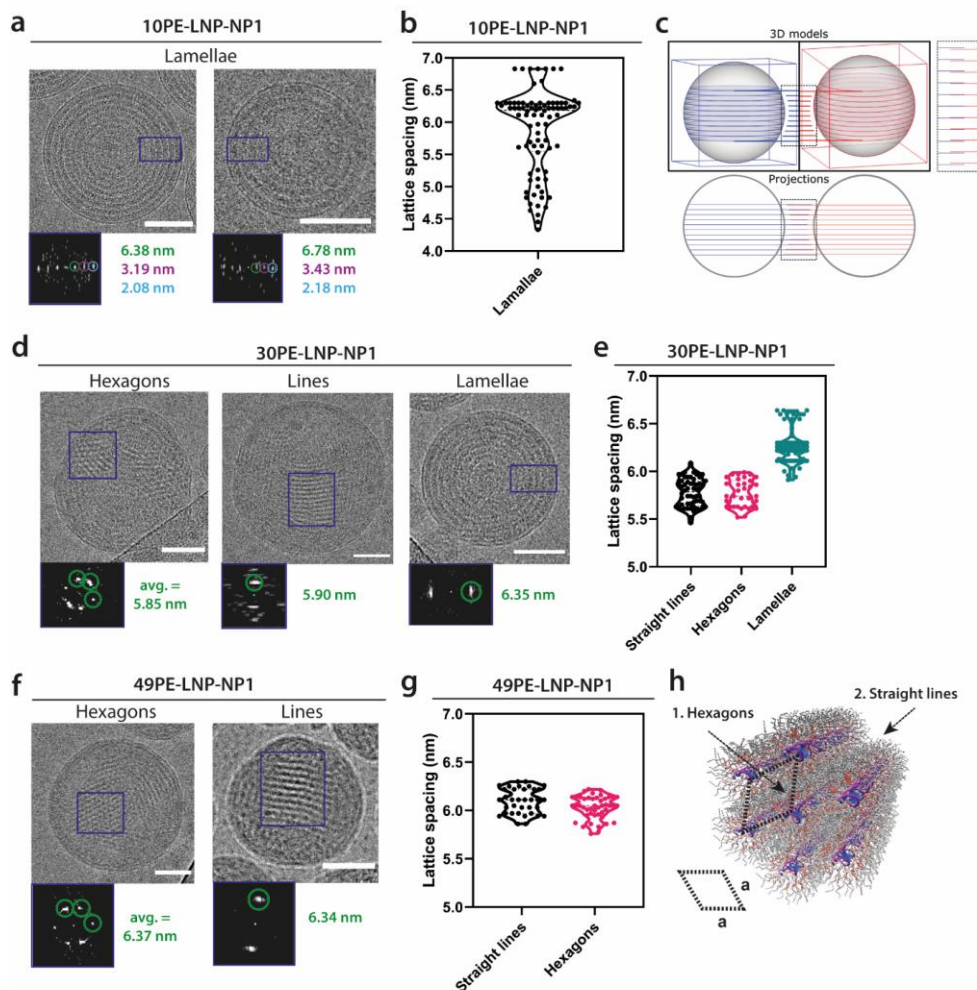

Figure 2. Identification and quantification of lipid-siRNA structures in LNPs. (a) cryoTEM of representative structures found in 10PE-LNP-NP1. FFT values represent the [100] structure and higher-order reflections. Scale bars are 50 nm. (**b**) Quantification of lamellar spacings (n = 84, 5.88 nm ± 0.65 nm, median = 6.18 nm). Values are derived from the first-order reflections in the FFT of 10PE-LNP-NP1. (**c**) Schematic representation of lamellar structures at different tilt angles. Projection of lattices shown in red appear narrower than blue due to out of plane rotation of the LNPs. Dashed box shows a magnification of the indicated regions. (**d**) CryoTEM of individual

104

particles displayed representative structures found in 30PE-LNP-NP1. Scale bars are 50 nm. (**e**) Quantification of lattice spacings of the different structures displayed in d: straight lines (n = 56, 5.78 nm ± 0.14 nm), hexagons (n = 34, 5.77 nm ± 0.14 nm) and lamellae (n = 78, 6.26 nm ± 0.18 nm). (**f**) CryoTEM of individual particles displaying representative structures found in 49PE-LNP-NP1. Scale bars are 50 nm. (**g**) Quantification of lattice spacings of the different structures displayed in f: hexagons (n = 46, 6.03 ± 0.12 nm) and straight lines (n = 35, 6.10 ± 0.13 nm). (**h**) Atomistic model of inverse hexagonal lipid structures with associated primitive cell. The lattice spacings derived from cryoTEM images are denoted as **a.**

Following identification and characterization of paracrystalline inverse hexagonal structures inside of LNPs using combined SAXS and cryoTEM, we sought to investigate the effect of siRNA content on the assembly pathway and three-dimensional architecture of the LNPs. Assembly of 49PE-LNPs without siRNA (49PE-LNP-noRNA) or with an NP ratio of 6 (49PE-LNP-NP6) both yielded straight lines and hexagonal structures similar to 49PE-LNP-NP1, but with different dimensions (**Figure 3a, Figure S7**). Single particle lattice spacing analysis on these structures revealed a single population for 49PE-LNP-noRNA with an average lattice spacing of 4.78 nm ± 0.11 nm, and a bimodal distribution for 49PE-LNP-NP6 with an average of 4.84 nm ± 0.16 nm for the lower population and an average of 6.20 nm ± 0.17 nm for the higher population (**Figure 3b**). The lattice spacing of the lower population of the 49PE-LNP-NP6 is highly similar to the 49PE-LNP-noRNA distribution, whereas the lattice spacing of the higher population is highly similar to that of 49PE-LNP-NP1. This widening of the lattice spacing for the higher distribution of 49PE-LNP-NP6 and 49PE-LNP-NP1 over that of the lower population of 49PE-LNP-NP6 and 49PE-LNP-noRNA is due to encapsulation of siRNA within in the tubular structure, with the change being close to the calculated width (~2 nm) of a free siRNA molecule (**Figure S1b**). These therefore represent 'empty' and 'filled' hexagonally-packed tubular structures (**Figure 3c**).

Furthermore, no combination of 'empty' and 'filled' structures within the same LNP was observed with cryoTEM, suggesting that a non-saturating amount of siRNA during assembly gives rise to two parallel assembly pathways. DLS measurements indicated that 49PE-LNPs assembled without siRNA are larger and more polydisperse in dimension than LNPs assembled with a NP ratio of 1 (**Table S2**). To examine this more closely, we compared the particle diameters of 'empty' and 'filled' 49PE-LNP variants determined by cryoTEM (**Figure S9**). In line with the DLS results, we found that 'filled' LNPs tend to be smaller and more monodisperse (D = 117 nm ± 33 nm and D = 118 nm ± 22 nm for 49PE-LNP-NP6-filled and 49PE-LNP-NP1, respectively) than 'empty' particles (D = 224 nm ± 70 nm and D = 257 nm ± 95 nm for 49PE-LNP-NP6-empty and 49PE-LNP-noRNA, respectively). In addition, 49PE-LNP-noRNA shows the formation of empty tubular

structures throughout the LNP core that were longer than the filled structures in the case of 49PE-LNP-NP1 (**Figure S7b,d**). Although the exact mechanisms underlying LNP assembly remain elusive and beyond the scope of this work,[15,42,46] we hypothesize that DODAP and DOPE can form inverted hexagonal phases in the absence of siRNA, leading to the formation longer tubular structures which in turn favors the formation of larger LNPs. In the presence of siRNA, which is ~5 nm in length, the formation of long tubular structures requires the alignment of multiple siRNA molecules that, along with the electrostatic interaction between DODAP and siRNA, make it more prone to disruption and leads to the formation of smaller LNPs with paracrystalline order comprising shorter tubes.

In addition to the inverse hexagonal tubular structures formed in 49PE-LNP-noRNA, we also identified a spherical structure that was able to co-exist in the same particle with inverse hexagonal tubular structures (**Figure S10a**). CryoET revealed the formation of two independent structures within the same LNP, and showed that the spheres resided at the periphery, in regions without inverse hexagonal tubes (**Figure 3d,e**). In addition, cryoET slices of an individual LNP showed that these spherical structures with a size of ~8-10 nm can be hexagonally packed (**Figure S11**). These spheres are reminiscent of an inverse micellar phase with an aqueous core.[47] In our case, inverse micelles consisting of DODAP and DOPE with the hydrophobic tails point outwards surrounding a large aqueous core accurately reflect the formed structure. In order to determine to what end the SAXS profiles reflected the formed phases we calculated the d-spacing using of the q_{max} values for each of the distinguishable peaks. Due to the co-existence of phases, the first and second order Bragg peaks could reflect [1,0] and [1,1] of one of the structures, or the [1,0] and [1,0] of the two individual hexagonally packed structures (spheres or tubes) (**Figure S10b**). Assuming a single structure, an average d-spacing of 8.48 nm was found, closely reflecting the average size of the inverse micellar structures identified in cryoET (**Figure S10c,d**), whilst calculations assuming two structures revealed that the d-spacing of the second order peak was ~4.95 nm, similar to the average lattice spacing of the inverse hexagonal tubular structures derived from cryoTEM (**Figure 3b**). Together, these results indicate that the peaks in the SAXS profiles represent an overlap of two coexisting structures. Although the resolution of SAXS may be insufficient for the accurate determination of multiple coexisting structural states, it still serves as a qualitative bulk measurement for the relative comparison of structural changes between LNP formulations. Furthermore, the increased lattice spacing in the case of 49PE-LNP-NP1 compared to 49PE-LNP-noRNA is confirmed by a shift in the SAXS profile to lower q_{max} values, of which the same analysis yields and average d-spacing of 6.22 nm (**Figure S10e,f**). A similar shift of the first order peak was observed, suggesting the presence of hexagonally packed spheres with an average d-spacing

of 10.71 nm in the case of 49PE-LNP-NP1. However, inverse micellar structures as found in 49PE-LNP-noRNA were not identified in the case of 49PE-LNP-NP1 using cryoTEM. Nevertheless, we did identify polymorphic-like structures that appear as disordered in cryoTEM (**Figure S10g,h**). Since the particles of 49PE-LNP-NP1 are significantly smaller than 49PE-LNP-noRNA, the identification of ~10 nm structures might be problematic in cryoTEM due to the lack of space at the LNP periphery, leading to a decreased repeatability and less order.

To explore the structural organization in 49PE-LNP-NP1, we used cryoET and identified the polymorphic and inverse hexagonal structures within a single LNP (**Figure 3f**). Inverse hexagonally packed structures were present throughout the core of the LNP, whereas the amorphous structures appeared on the LNP periphery, similar to the spherical structures in 49PE-LNP-noRNA, where they form an interface between the well-ordered core and amorphous lipid membrane. Isosurface reconstruction of the tomogram reveals the paracrystalline nature of the inverse hexagonal phases, appearing in both straight lines and hexagonal orientations within the same particle (**Figure 3g**). The electron density of the tomogram fitted with a siRNA-lipid structure (50:50 mol% DODAP:DOPE) shows a clear overlap of the maximum electron density with the siRNA molecules (**Figure 3h**). Altogether, these results confirm the successful assembly of inverse hexagonal phases, encapsulating siRNA, in the core of LNPs.
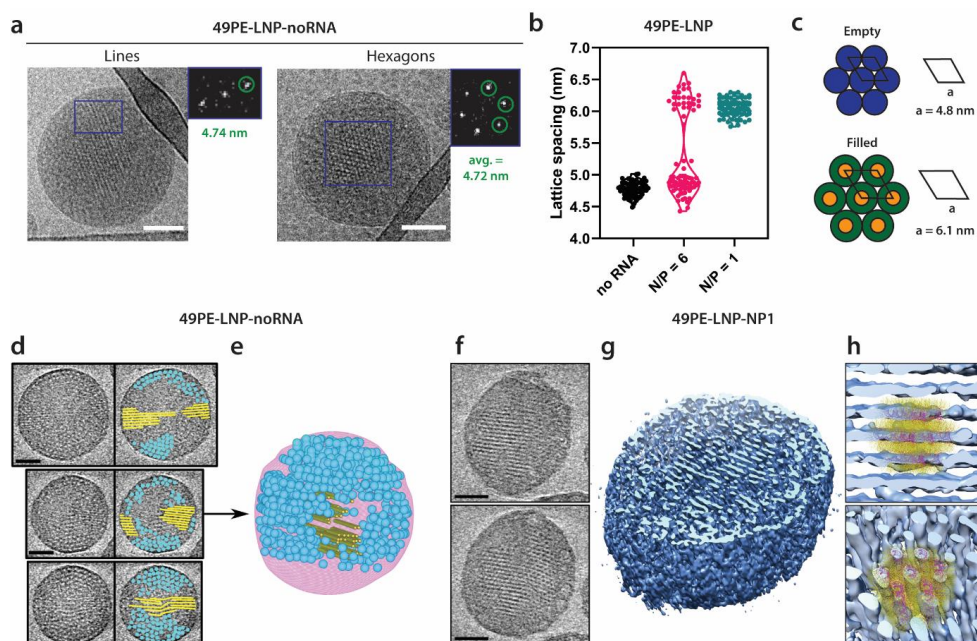
Figure 3. Identification of filled and empty inverse hexagonal structures. (**a**) Representative cryoTEM and FFTs of 49PE-LNP-noRNA showing two distinct structures: straight lines and hexagons. Scale bars are 50 nm. (**b**) Quantification of lattice spacings of structures found in 49PE-LNP at different RNA amounts: no RNA (n = 63, 4.78 nm ± 0.11 nm), NP = 6 (total: n = 77, 5.31 nm ± 0.67, low population: n = 50, 4.84 nm ± 0.16 nm, high population: n = 27, 6.20 nm ± 0.17 nm) and NP = 1 (n = 81, 6.06 nm ± 0.13 nm). (**c**) Schematic representation of 'empty' and 'filled' inverted hexagonal structures. (**d**) CryoET slices of 3 separate 49PE-LNP-noRNA particles. Identified spherical and tubular structures in each slice are indicated as blue circles and yellow lines respectively. Scale bars are 50 nm. (**e**) Reconstruction of the three-dimensional tomogram shown as the middle LNP in d. (**f**) CryoET slices through an individual 49PE-LNP-NP1 particle. EM images represent slices at two different heights of the tomogram, showing straight lines (top) and hexagonally packed regions (bottom). Scale bars are 50 nm. (**g**) Surface rendering indicates internal paracrystalline structures. (**h**) Fitted siRNA-lipid models to the electron density derived from cryoET, showing different orientations of the same structure (RNA in purple, lipid tails in yellow).

The formation and characterization of LNPs is typically performed and reported at room temperature (RT, 25 °C). However, once applied at a physiological temperature (37 °C), the change in temperature can influence lipid structures and LNP performance. Therefore, we explored the stability of the lipid superstructures in 10PE-LNP-NP1, 30PE-LNP-NP1 and 49PE-LNP-NP1 at these temperatures using SAXS. Each LNP sample was subjected to three 6h measurements and two 1h temperature ramps to collect data at 25 °C before heating to 37 °C, and once again at 25 °C after heating. Interestingly, the Bragg reflection characteristic for the lamellar structure in 10PE-LNP-NP1 was only visible at room temperature before heating, while it was completely abolished at 37 °C and did not recover upon cooling down back to room temperature (**Figure 4a**). In addition, no other Bragg reflections were observed. The loss of the lamellar structure and its transformation into a more disordered phase thus appears irreversible. By contrast, neither 30PE-LNP-NP1 nor 49PE-LNP-NP1 exhibited a significant change in their SAXS profiles collected at 25°C and 37 °C (**Figure 4b,c**).

As a control formulation, we designed a LNP that would maintain its lamellar structure upon heating to 37 °C. We hypothesized that substitution of the ionizable lipid DODAP in 10PE-LNP-NP1 with its fully saturated analogue 1,2-distearoyl-3-dimethylammonium-propane (DSDAP), while keeping the rest of the lipids and NP ratio constant, would increase the overall transition temperature of the LNP formulation and lead to the formation of rigid lamellar structures (10PE-DS-LNP-NP1, **Figure 4d,e**). This formulation showed a similar scattering signal compared to 10PE-LNP-NP1 at 25 °C, but no significant decrease when measured at 37 °C or after heating at 25 °C (**Figure 4f**). We probed the dynamic structural changes in 10PE-LNP-NP1 and 10PE-DS-LNP-NP1 by collecting SAXS

profiles at 25 °C, followed by measurements at 37 °C in intervals of 1 hour over a total time of 12 hours (**Figure 4g,h and Figure S12**). For 10PE-LNP-NP1, the scattering signal decreased rapidly after 1 hour and was largely absent after 3-4 hours, whereas the scattering signal for 10PE-DS-LNP-NP1 remained generally unchanged over the complete 12-hour period. To confirm and visualize the structural changes in 10PE-LNP-NP1, cryoTEM imaging was performed after incubation for 1 hour at 37 °C, revealing the formation of polymorphic and amorphous structures, with a small amount of lamellar structure still present (**Figure 4i**). For 10PE-DS-LNP-NP1, cryoTEM imaging showed the formation of spherical and disk-like LNPs containing lamellar structures at 25 °C (**Figure 4j**). Notably, lamellar structures were not present as concentric rings that extended to the core of the LNP, as found in 10PE-LNP-NP1, but instead showed the formation of amorphous structure in the LNP core. This is likely due to the severe decrease in bending capability of lamellar structures containing the saturated and rigid DSDAP lipid. In addition, the observed structures of 10PE-DS-LNP-NP1 remained visible after a 1-hour incubation at 37 °C (**Figure 4k**), in agreement with the respective SAXS profiles.
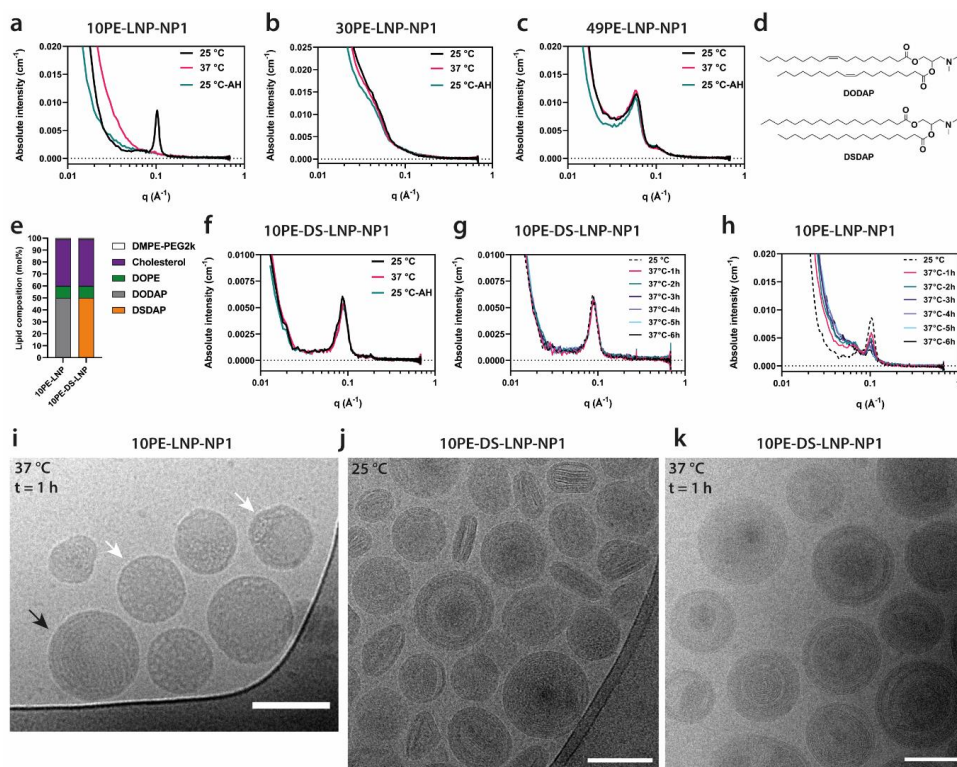
Figure 4. The effect of temperature on LNP core structure. (**a-c**) SAXS profiles of LNP-10PE-NP1, LNP-30PE-NP1 and LNP-49PE-NP1 at 25 °C, 37 °C and 25 °C after heating (AH) (**d**) Chemical structures of the ionizable lipids DODAP and DSDAP (**e**) Lipid compositions for the rigidification of thermolabile lamellar 10PE-LNP-NP1 to a rigid formulation 10PE-DS-LNP-NP1. (**f**) SAXS profiles of 10PE-DS-LNP-NP1 at 25 °C, 37 °C and 25 °C after heating (AH) (**g,h**) SAXS profiles 10PE-DS-LNP-NP1 and 10PE-LNP-NP1 at 25 °C, and at 1 hour intervals at 37 °C. (**i**) CryoTEM of 10PE-LNP-NP1 after incubation at 37 °C for 1 hour. White arrows indicate the formation of polymorphic and amorphous structures, black arrows indicate lamellar structure. Scale bar is 100 nm. (**j,k**) CryoTEM of 10PE-DS-LNP-NP1 at 25 °C and after incubation at 37 °C for 1 hour. Scale bars are 100 nm.

After characterization of LNPs, we assessed the intracellular silencing efficiency of LNPs containing rigid lamellar (10PE-DS-LNP-NP1), thermolabile lamellar (10PE-LNP-NP1), mixed (30PE-LNP-NP1) or paracrystalline inverted hexagonal phases (49PE-LNP-NP1). The efficiency of LNP mediated transfection was determined by the silencing of GFP tagged to the endogenous proteins CD63 and UBE2I, in HeLa and U2OS cells respectively.[48,49] In order to monitor the difference in uptake between formulations, a small amount of the non-exchangeable lipid dye 1,1′-dioctadecyl-3,3,3′,3′-tetramethylindodicarbocyanine (DiD, 0.1 mol%) was added to the formulations during formation. These LNPs, encapsulating the siRNA for GFP, were added to the cells at various doses of encapsulated siRNA (0 – 83 nM) and incubated for 24 hours, after which the medium was refreshed and the cells were allowed to grow for another 48 hours in order to deplete the GFP that was expressed before the addition of LNPs (**Figure 5a**). At 72 hours, the cells were collected and fluorescence-activated cell sorting (FACS) was performed to quantify both the absolute uptake of LNPs, based on the mean fluorescence intensity (MFI) of the DiD dye, and the silencing efficiency relative to PBS treated cells from the MFI of GFP. A colorimetric cell-viability study (MTT) performed at 72 hours showed that the viability of both cultured cell lines remained unaffected by any of the LNP formulations across all doses (**Figure S13**).

For the U2OS-UBE2I-GFP cell line, uptake of LNPs was similar in all cases up to 50 nM (**Figure 5a**), but clear differences in GFP fluorescence were observed (**Figure 5b**). Here, 49PE-LNP-NP1 showed the most GFP silencing across all doses, followed by LNP-30PE-NP1 and LNP-10PE-NP1. Finally, the rigid lamellar LNP-10PE-DS-NP1 showed poor transfection relative to the other formulations, where only the highest concentration of 83 nM led to more than 50% GFP silencing. For the latter, this observation of increased saturation in ionizable cationic lipids leading to less efficient cellular transfection closely reflects previous reports.[50] In the HeLa-CD63-eGFP cell line, similar uptake and silencing efficiency trends were observed for all formulations up to 25 nM (**Figure 5c**). Similar trends

of silencing efficiency were observed to the U2OS cell line, in which 49PE-LNP-NP1 and 30PE-LNP-NP1 performed the best, despite lower cellular uptake at higher doses (50 nM and 83 nM). However, in this cell line, 10PE-LNP-NP1 and 10PE-DS-LNP-NP1 exhibited similar silencing efficiencies suggesting that there is little difference in silencing between the rigid and thermo-labile lamellar structures.
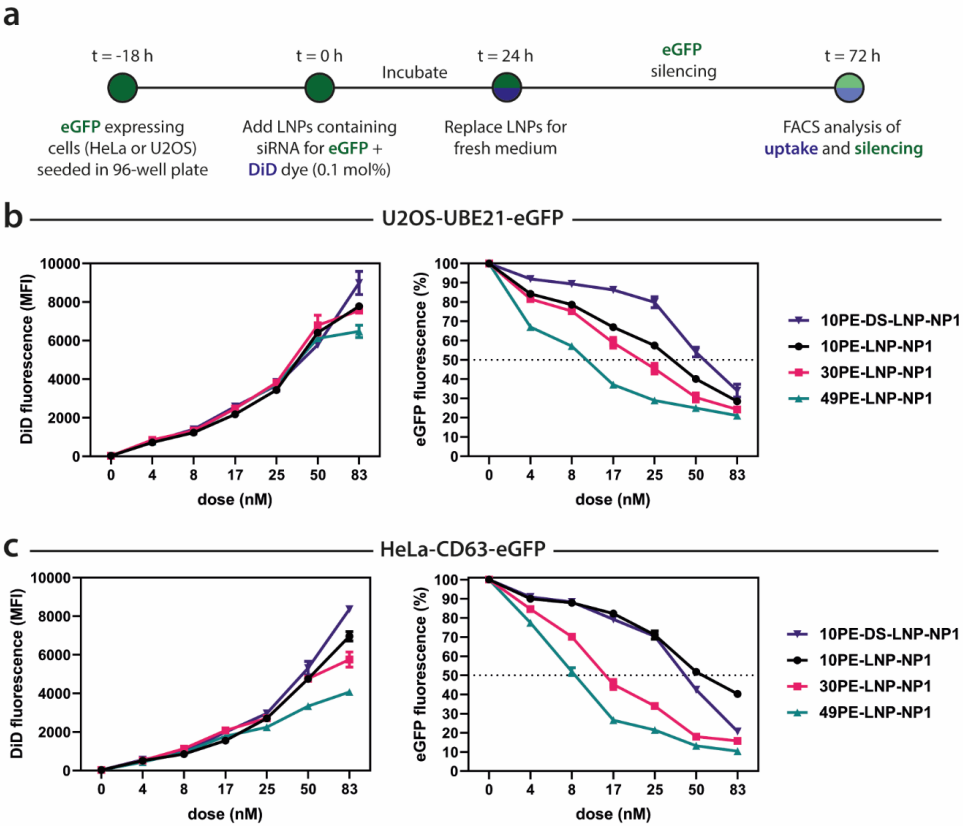

Figure 5. Intracellular silencing of eGFP with lamellar and paracrystalline inverted hexagonal LNPs. (**a**) Schematic representation of the cell culture eGFP silencing experiment. Cells are incubated with LNPs for 24 hours, followed by medium replacement and culturing for an additional 48 hours. At 72 hours, the cells are collected and analyzed using FACS for LNP uptake and eGFP silencing. (**b,c**) LNP uptake and eGFP silencing in U2OS-UBE21-eGFP or HeLa-CD63-eGFP cell lines. LNP uptake is quantified based on the mean fluorescence intensity (MFI) of DiD in the cells. The relative eGFP fluorescence (%) is quantified as the MFI of GFP in the treated cells compared to PBS treated cells. All data points are the average of a triplicate and error bars reflect the standard deviation.

After establishing a clear trend in transfection efficiency when comparing LNPs with defined lipid structures, we sought to gain more mechanistic insights into the LNP-membrane interaction. Interactions between LNPs and endosomal membranes are driven by an electrostatic interaction of negatively charged membranes and protonated LNPs in an acidic endosomal environment.[17] Therefore, we studied the interaction of LNPs with anionic large unilamellar vesicles (LUVs) that mimic endosomal membranes. The lipid composition of endosomal membranes is complex, dynamic and dependent on cell type, typically rich in (zwitterionic) neutral lipids such as phosphatidylcholine (PC), phosphatidylethanolamine (PE) and cholesterol (Chol),[51] along with lipids that have a formal negative charge such as phosphatidylserine (PS) and phosphatidylinositol (PI).[52,53] A lipid composition of PC:PE:PS:Chol:PI at a ratio of 50:27:10:10:3 mol% was chosen, where purified lipid extracts with variable lipid chain lengths for each of the phospholipids were used, to reflect the high variability of lipid chain length and saturation in natural membranes (see **Supplementary Information**). These unilamellar model membranes were assembled using thin-film hydration, followed by multiple freeze-thawing cycles and extrusion. CryoTEM, DLS and Zeta Potential measurements confirmed the formation of monodisperse anionic LUVs of ~100-150 nm (**Figure S14, Table S2**).

We first sought to investigate the effect that the different LNP lipid compositions had on lipid mixing with our model membranes. To this end, we added two DOPE lipid-conjugated fluorophores, Nitrobenzoxadiazole (PE-NBD) and Lissamine Rhodamine B (PE-LR) to the composition of the LUVs at 1.5 mol% each, substituting for PE. These fluorophores form a Fluorescence Resonance Energy Transfer (FRET) pair, in which PE-LR quenches the fluorescence of PE-NBD when they are in close proximity. Upon lipid mixing between LNP and LUVs, the lipid-conjugated fluorophores will be separated leading to dequenching of the PE-NBD fluorescence over time (**Figure 6a**). When lipid mixing was performed at a typical endosomal pH of 6.0 at 37 °C,[54] all LNPs displayed lipid mixing with the acceptor liposomes, but a clear trend was observed showing that an increase in DOPE content displayed faster lipid mixing kinetics as well as a higher total lipid mixing efficiency (**Figure 6b**). Furthermore, the rigid lamellar formulation LNP-10PE-DS-NP1 showed the lowest lipid mixing kinetics and efficiency. In all cases, no active lipid mixing was observed at a physiological pH of 7.4 at 37 °C, confirming the need for a pH below the pKa of DODAP for the initiation of the LNP-LUV interaction (**Figure 6b**). The trend of lipid mixing efficiency closely correlates to the observed silencing efficiencies observed in cell culture (**Figure 4b,c**), where 49PE-LNP-NP1 is the most efficient for both lipid mixing and silencing.

Next, we explored the alteration of the defined lipid structures upon lipid mixing of LNPs with LUVs. Judging from the FRET based assay, lipid mixing reached an equilibrium after

~30 minutes. Therefore, we visualized the LNP-LUV interaction with cryoTEM after 1 and 7 hours and used SAXS in the intermediate period of 6 hours to determine the preservation of defined lipid structures (**Figure 6c**). The very inefficient lipid mixing of 10PE-DS-LNP-NP1 was reflected in the SAXS profile, showing a minor decrease in lamellar signal compared to 10PE-DS-LNP-NP1 before mixing (**Figure S15a,b**). In addition, cryoTEM revealed the docking of LNPs to LUVs but lacking further fusion or structural change, at both 1 and 7 hours. (**Figure S15c,d**).

In the case of 10PE-LNP-NP1, the respective SAXS profile showed a decrease in the lamellar signal after mixing (**Figure 6d**). The SAXS profile also shows the increase of a distinguishable peak at a lower q-value, suggesting the formation of additional structures. CryoTEM revealed that these LNPs interact with LUVs and form inverted hexagonal structures at the LNP-LUV interface, while also retaining characteristics of lamellar structures as determined by FFT analysis (**Figure 6f, Figure S17**). Furthermore, these structures remain visible after incubation with LUVs after 7 hours, indicating preservation of the lipid structures. The first order peaks of both lamellar and inverse hexagonal structures will appear as a signal at a q-value of ~0.1, making it difficult to distinguish the contribution of these structures to the observed signal. Nevertheless, a complete abolishment of the lamellar structures as seen for 10PE-LNP-NP1 alone is not observed, indicating that the thermal stability of these structures is increased upon lipid mixing with the acceptor LUVs.

For 30PE-LNP-NP1 mixed with LUVs, the measured SAXS profile showed complete abolishment of the broad 30PE-LNP-NP1 signal present before mixing while primarily yielding a signal at a q-value of ~0.1 (**Figure S16a,b**). CryoTEM at both 1 and 7 hours show the primary formation of inverted hexagonal structures and straight lines, although some lamellar structures were also identified (**Figure S16c,d**). Finally, for 49PE-LNP-NP1, the SAXS profile showed the complete abolishment of the signal corresponding to the first order signal of the larger structures, yielding a clearly defined peak corresponding to the first order peak of the inverse hexagonal tubular structures (**Figure 6e, Figure S10e**). CryoTEM showed the sole formation of crystalline inverse hexagonal phases, visualized as hexagons or straight lines (**Figure 6g, Figure S18**). Furthermore, these structures remained clearly visible after 7 hours, confirming preservation upon interaction with LUVs and the thermal stability of these structures.

From these results, we propose a mechanism that explains the observations of enhanced lipid mixing and transfection of LNPs with paracrystalline inverse hexagonal over lamellar phases, and to what extent it might impact intracellular siRNA delivery (**Figure 6h**). After

an initial interaction of LNPs with acceptor LUVs triggered by the protonation of ionizable lipids (ILs) at acidic pH, the LNPs follow two different pathways for the delivery of their cargo. In the case of 10PE-LNP-NP1, an *in situ* transition of lamellar to inverse hexagonal phase takes place at the LNP-LUV intersection, which allows for membrane disruption and the eventual escape of RNA molecules from the LNP (**Figure 6h, pathway 1**). These findings are complementary to the rationale for which membrane-disrupting ILs or LNP formulations were designed, in which ILs form non-lamellar structures with the anionic lipids of the acceptor membrane.[18,19] Other factors that will play a role in LNPs with lamellar structures can be the overall fluidity of the lipid mixture and the pKa of the IL. [22,25] Although the formation of pre-programmed inverse hexagonal phases in LNPs has not been reported before, permanently cationic lipid-oligonucleotide complexes, named lipoplexes, show a degree of similarity to our system.[55–57] Here, lipoplexes containing inverse hexagonal phases encapsulating double-stranded DNA (dsDNA) interacting with acceptor giant unilamellar vesicles (GUVs, ~20 μm) are shown to generate near complete lipid mixing towards a lamellar acceptor membrane.[44] However, the visualization of lipoplex-membrane complexes at the nanoscale has not been reported. More recently, molecular dynamics simulations of inverse hexagonal lipoplexes containing dsDNA interacting with anionic membranes show how dsDNA is able to escape from the lipoplex.[58] These results align directly with our observation of retention of the pre-programmed inverse hexagonal phase upon interaction with the LUVs. Therefore, derived from our cryoTEM and SAXS data, we suggest that these structures bypass the initial lamellar-to-inverse hexagonal phase transition that is occurring for 10PE-LNP-NP1, instead generating a more efficient 1-step process of siRNA delivery directly from the inverse hexagonal phase (**Figure 6h, pathway 2**). An important observation is, although the presence of paracrystalline H_{II} phases improves lipid mixing and transfection efficiency, complete fusion of the LNP-LUV systems does not occur, leaving a large amount of siRNA complexed in thermodynamically stable siRNA-lipid structures. Although our *in vitro* model is a simplified version of the LNP-membrane interaction and lacks the presence of the complex dynamic intracellular environment, these observations and proposed mechanism may provide a contributing factor to the poor endosomal escape of RNA molecules ($\leq 2\%$) from the endosome into the cytosol.[17,20,21]
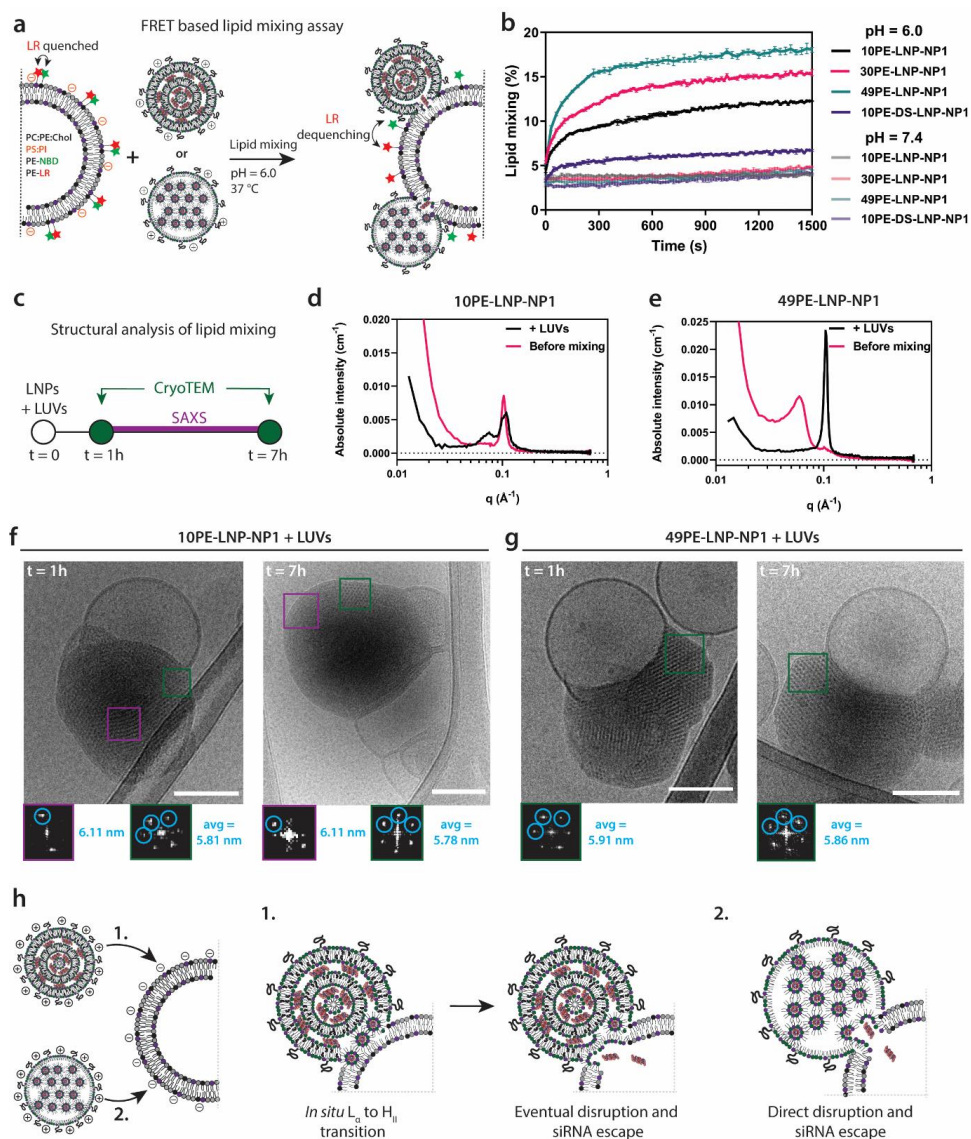
Figure 6. Interaction of LNPs with anionic LUVs. (**a**) Schematic representation of the FRET based lipid mixing assay. LNPs are mixed with anionic acceptor liposomes containing two lipid conjugated fluorophores (PE-NBD and PE-LR), after which the dequenching of PE-NBD is measured over time. (**b**) Lipid mixing results of LNPs (250 μM) mixed with anionic LUVs (125 μM) at pH 6.0 and 7.4 cryoTEM, performed at 37 °C for 25 minutes. Plotted data is the average of a triplicate in which error bars represent the standard deviation. (**c**) Schematic representation of the structural analysis of lipid

mixing between LNPs and LUVs. CryoTEM imaging was performed after an incubation of 1 hour at 37 °C. Similarly, SAXS measurements over a time span of 6 hours were started after an incubation of 1 hour at 37 °C. (**d,e**) SAXS profiles of 10PE-LNP-NP1 or 49PE-LNP-NP1 mixed with LUVs. (**f,g**) Representative cryoTEM images of 10PE-LNP-NP1 or 49PE-LNP-NP1 mixed with LUVs. Scale bars are 100 nm (**h**) Schematic representation of a proposed mechanism explaining the increased lipid mixing and transfection efficiency of LNPs with pre-programmed inverse hexagonal phases compared to LNPs with lamellar phases.

5.3 Discussion

Using bottom-up rational design of defined lipid superstructures, we have generated LNPs with paracrystalline inverse hexagonal lipid structures actively encapsulating siRNA and with enhanced transfection efficiency over LNPs containing lamellar structures. Due to the inherent complexity of lipid behavior in LNPs during and after nanoparticle assembly, an in-depth characterization combining cryoTEM, SAXS and cryoET was employed to determine the effects of lipid composition, RNA content, temperature and membrane interaction on the formation and stability these structures. Endosomal escape remains a tremendous barrier for the improvement of LNP-based RNA therapeutics, yet our data shows that, through inducing pre-programmed lipid phases, transfection efficiency can be enhanced. This may play a crucial role for widespread applications. Here, it is important to recognize the extensive efforts in the exploration of the chemical space of ionizable lipids[24,25,59], and other LNPs components for the promotion of endosomal escape of RNA molecules.[33,34] Since the formation of non-lamellar lipid structures is driven by total lipid composition of these multicomponent systems, and therefore not exclusively on specific ILs, we believe that our approach for inducing inverse hexagonal structures can be retrofitted to LNPs with other ILs or components, albeit it at different lipid concentrations or RNA content, to increase their LNP potency, which will allow additional exploration of the structural space of LNPs. Consequently, the large variety of natural and synthetic lipids also generates possibilities for the rational design of other defined lipid structures.[36,60,61]

LNPs are currently applied in a widespread of LNP-RNA therapeutic approaches,[62–65] for example in the form of prophylactic vaccines against COVID-19.[11,12,66,67] It will be of great interest to expand the defined structural space of LNPs containing RNA molecules with a more complex and less predictable structure than siRNA (*e.g.* mRNA and single guide RNA). To this end, bottom-up approaches of LNP design and application, based on rational design and the mechanistic understanding of the nano-bio interactions, can help to predict and understand of these structures. Finally, mechanistic knowledge about lipid superstructures containing RNA molecules, and their behavior with endosomal

membranes, will enable the predictions of LNP potency from a bottom-up based approach in which LNP formulations are assessed with biophysical methods before their application to *in vitro* or *in vivo* systems, opening up another avenue of LNP design and optimization.

5.4 References

1. Delivering the promise of RNA therapeutics. *Nat. Med.* **25,** 1321 (2019).
2. Lieberman, J. Tapping the RNA world for therapeutics. *Nat. Struct. Mol. Biol.* **25,** 357–364 (2018).
3. Wang, F., Zuroske, T. & Watts, J. K. RNA therapeutics on the rise. *Nature reviews. Drug discovery* **19,** 441–442 (2020).
4. Yin, H. *et al.* Non-viral vectors for gene-based therapy. *Nat. Rev. Genet.* **15,** 541–555 (2014).
5. Nguyen, J. & Szoka, F. C. Nucleic acid delivery: the missing pieces of the puzzle? *Acc. Chem. Res.* **45,** 1153–1162 (2012).
6. Jones, C. H., Chen, C. K., Ravikrishnan, A., Rane, S. & Pfeifer, B. A. Overcoming nonviral gene delivery barriers: Perspective and future. *Mol. Pharm.* **10,** 4082–4098 (2013).
7. Cullis, P. R. & Hope, M. J. Lipid Nanoparticle Systems for Enabling Gene Therapies. *Mol. Ther.* **25,** 1467–1475 (2017).
8. Rajabi, M. & Mousa, S. A. Lipid Nanoparticles and their Application in Nanomedicine. *Curr. Pharm. Biotechnol.* **17,** 662–672 (2016).
9. Akinc, A. *et al.* The Onpattro story and the clinical translation of nanomedicines containing nucleic acid-based drugs. *Nat. Nanotechnol.* **14,** 1084–1087 (2019).
10. Adams, D. *et al.* Patisiran, an RNAi therapeutic, for hereditary transthyretin amyloidosis. *N. Engl. J. Med.* **379,** 11–21 (2018).
11. Jackson, L. A. *et al.* An mRNA Vaccine against SARS-CoV-2 — Preliminary Report. *N. Engl. J. Med.* **383,** 1920–1931 (2020).
12. McKay, P. F. *et al.* Self-amplifying RNA SARS-CoV-2 lipid nanoparticle vaccine candidate induces high neutralizing antibody titers in mice. *Nat. Commun.* **11,** 3523 (2020).
13. Evers, M. J. W. *et al.* State-of-the-Art Design and Rapid-Mixing Production Techniques of Lipid Nanoparticles for Nucleic Acid Delivery. *Small methods* **1700375,** 1–20 (2018).
14. Leung, A. K. K., Tam, Y. Y. C., Chen, S., Hafez, I. M. & Cullis, P. R. Microfluidic Mixing: A General Method for Encapsulating Macromolecules in Lipid Nanoparticle Systems. *J. Phys. Chem. B* **119,** 8698–8706 (2015).
15. Kulkarni, J. A. *et al.* On The Formation and Morphology of Lipid Nanoparticles Containing Ionizable Cationic Lipids and siRNA. *ACS Nano* **12,** 4787–4795 (2018).
16. Arteta, M. Y. *et al.* Successful reprogramming of cellular protein production through mRNA delivered by functionalized lipid nanoparticles. *Proc. Natl. Acad. Sci. U. S. A.* **115,** E3351–E3360 (2018).
17. Wittrup, A. *et al.* Visualizing lipid-formulated siRNA release from endosomes and target gene knockdown. *Nat. Biotechnol.* **33,** 870–876 (2015).
18. Semple, S. C. *et al.* Rational design of cationic lipids for siRNA delivery. *Nat. Biotechnol.* **28,** 172–176 (2010).
19. Liu, S. *et al.* Membrane-destabilizing ionizable phospholipids for organ-selective mRNA delivery and CRISPR–Cas gene editing. *Nat. Mater.* **20,** 701–710 (2021).
20. Gilleron, J. *et al.* Image-based analysis of lipid nanoparticle–mediated siRNA delivery, intracellular trafficking and endosomal escape. *Nat. Biotechnol.* **31,** 638–646 (2013).

21. Sahay, G. *et al.* Efficiency of siRNA delivery by lipid nanoparticles is limited by endocytic recycling. *Nat. Biotechnol.* **31**, 653–658 (2013).

22. Jayaraman, M. *et al.* Maximizing the potency of siRNA lipid nanoparticles for hepatic gene silencing in vivo. *Angew. Chemie - Int. Ed.* **51**, 8529–8533 (2012).

23. Lokugamage, M. P., Sago, C. D., Gan, Z., Krupczak, B. R. & Dahlman, J. E. Constrained Nanoparticles Deliver siRNA and sgRNA to T Cells In Vivo without Targeting Ligands. *Adv. Mater.* **31**, 1902251 (2019).

24. Miao, L. *et al.* Delivery of mRNA vaccines with heterocyclic lipids increases anti-tumor efficacy by STING-mediated immune cell activation. *Nat. Biotechnol.* **37**, 1174–1185 (2019).

25. Rietwyk, S. & Peer, D. Next-Generation Lipids in RNA Interference Therapeutics. **11**, 7572–7586 (2017).

26. Love, K. T. *et al.* Lipid-like materials for low-dose, in vivo gene silencing. *Proc. Natl. Acad. Sci.* **107**, 9915–9915 (2010).

27. Whitehead, K. A. *et al.* Degradable lipid nanoparticles with predictable in vivo siRNA delivery activity. *Nat. Commun.* **5**, 1–10 (2014).

28. Cheng, X. & Lee, R. J. The role of helper lipids in lipid nanoparticles (LNPs) designed for oligonucleotide delivery. *Advanced Drug Delivery Reviews* **99**, 129–137 (2016).

29. Kulkarni, J. A., Witzigmann, D., Leung, J., Tam, Y. Y. C. & Cullis, P. R. On the role of helper lipids in lipid nanoparticle formulations of siRNA. *Nanoscale* **11**, 21733–21739 (2019).

30. Chen, S. *et al.* Influence of particle size on the in vivo potency of lipid nanoparticle formulations of siRNA. *J. Control. Release* **235**, 236–244 (2016).

31. Paunovska, K. *et al.* A Direct Comparison of in Vitro and in Vivo Nucleic Acid Delivery Mediated by Hundreds of Nanoparticles Reveals a Weak Correlation. *Nano Lett.* **18**, 2148–2157 (2018).

32. Chen, S. *et al.* Development of lipid nanoparticle formulations of siRNA for hepatocyte gene silencing following subcutaneous administration. *J. Control. Release* **196**, 106–112 (2014).

33. Patel, S. *et al.* Naturally-occurring cholesterol analogues in lipid nanoparticles induce polymorphic shape and enhance intracellular delivery of mRNA. *Nat. Commun.* **11**, 983 (2020).

34. Eygeris, Y., Patel, S., Jozic, A. & Sahay, G. Deconvoluting Lipid Nanoparticle Structure for Messenger RNA Delivery. *Nano Lett.* **20**, 4543–4549 (2020).

35. Marsh, D. Intrinsic curvature in normal and inverted lipid structures and in membranes. *Biophys. J.* **70**, 2248–2255 (1996).

36. Zhai, J., Fong, C., Tran, N. & Drummond, C. J. Non-Lamellar Lyotropic Liquid Crystalline Lipid Nanoparticles for the Next Generation of Nanomedicine. *ACS Nano* **13**, 6178–6206 (2019).

37. Mouritsen, O. G. Lipids, curvature, and nano-medicine. *Eur. J. Lipid Sci. Technol.* **113**, 1174–1187 (2011).

38. Marrink, S. J. & Mark, A. E. Molecular view of hexagonal phase formation in phospholipid membranes. *Biophys. J.* **87**, 3894–3900 (2004).

39. Hu, B. *et al.* Therapeutic siRNA: state of the art. *Signal Transduct. Target. Ther.* **5**, 101 (2020).

40. Lipfert, J. *et al.* Double-stranded RNA under force and torque: Similarities to and striking differences from double-stranded DNA. *Proc. Natl. Acad. Sci.* **111**, 15408–15413 (2014).

41. Belliveau, N. M. *et al.* Microfluidic Synthesis of Highly Potent Limit-size Lipid Nanoparticles for In Vivo Delivery of siRNA. *Mol. Ther. Nucleic Acids* **1**, e37 (2012).

42. Kulkarni, J. A. *et al.* Spontaneous, solvent-free entrapment of siRNA within lipid nanoparticles. *Nanoscale* **12**, 23959–23966 (2020).

43. Rädler, J. O., Koltover, I., Salditt, T. & Safinya, C. R. Structure of DNA-Cationic Liposome Complexes: DNA Intercalation in Multilamellar Membranes in Distinct Interhelical Packing Regimes. *Science* **275**, 810–814 (1997).

44. Koltover, I., Salditt, T., Rädler, J. O. & Safinya, C. R. An Inverted Hexagonal Phase of Cationic Liposome-DNA Complexes Related to DNA Release and Delivery. *Science* **281**, 78–81 (1998).

45. Chen, Z. & Rand, R. P. The influence of cholesterol on phospholipid membrane curvature and bending elasticity. *Biophys. J.* **73**, 267–276 (1997).

46. Kulkarni, J. A. *et al.* Fusion-dependent formation of lipid nanoparticles containing macromolecular payloads. *Nanoscale* **11**, 9023–9031 (2019).

47. Shearman, G. C. *et al.* A 3-D Hexagonal Inverse Micellar Lyotropic Phase. *J. Am. Chem. Soc.* **131**, 1678–1679 (2009).

48. Jongsma, M. L. M. *et al.* An ER-Associated Pathway Defines Endosomal Architecture for Controlled Cargo Transport. *Cell* **166**, 152–166 (2016).

49. Qiao, X. *et al.* Uncoupling DNA damage from chromatin damage to detoxify doxorubicin. *Proc. Natl. Acad. Sci.* **117**, 15182–15192 (2020).

50. Heyes, J., Palmer, L., Bremner, K. & MacLachlan, I. Cationic lipid saturation influences intracellular delivery of encapsulated nucleic acids. *J. Control. Release* **107**, 276–287 (2005).

51. Symons, J. L. *et al.* Lipidomic atlas of mammalian cell membranes reveals hierarchical variation induced by culture conditions, subcellular membranes, and cell lineages. *Soft Matter* **17**, 288–297 (2021).

52. Yeung, T. *et al.* Membrane Phosphatidylserine Regulates Surface Charge and Protein Localization. *Science* **319**, 210–213 (2008).

53. Arumugam, S. & Kaur, A. The Lipids of the Early Endosomes: Making Multimodality Work. *Chembiochem* **18**, 1053–1060 (2017).

54. Maxfield, F. R. Role of endosomes and lysosomes in human disease. *Cold Spring Harb. Perspect. Biol.* **6**, a016931 (2014).

55. Ma, B., Zhang, S., Jiang, H., Zhao, B. & Lv, H. Lipoplex morphologies and their influences on transfection efficiency in gene delivery. *J. Control. Release* **123**, 184–194 (2007).

56. Safinya, C. R. *et al.* Cationic liposome-DNA complexes: From liquid crystal science to gene delivery applications. *Philos. Trans. R. Soc. A Math. Phys. Eng. Sci.* **364**, 2573–2596 (2006).

57. Majzoub, R. N., Ewert, K. K. & Safinya, C. R. Cationic liposome–nucleic acid nanoparticle assemblies with applications in gene delivery and gene silencing. *Philos. Trans. R. Soc. A Math. Phys. Eng. Sci.* **374**, 20150129 (2016).

58. Bruininks, B. M. H., Souza, P. C. T., Ingolfsson, H. & Marrink, S. J. A molecular view on the escape of lipoplexed DNA from the endosome. *Elife* **9**, e52012 (2020).

59. Hassett, K. J. *et al.* Optimization of Lipid Nanoparticles for Intramuscular Administration of mRNA Vaccines. *Mol. Ther. - Nucleic Acids* **15**, 1–11 (2019).

60. Amar-yuli, I. *et al.* Hexosome and Hexagonal Phases Mediated by Hydration and Polymeric Stabilizer. *Langmuir* **23**, 3637–3645 (2007).

61. Demurtas, D. *et al.* Direct visualization of dispersed lipid bicontinuous cubic phases by cryo-electron tomography. *Nat. Commun.* **6**, 1–8 (2015).

62. Pardi, N., Hogan, M. J., Porter, F. W. & Weissman, D. mRNA vaccines — a new era in vaccinology. *Nat. Rev. Drug Discov.* **17**, 261–279 (2018).

63. Trepotec, Z., Lichtenegger, E., Plank, C., Aneja, M. K. & Rudolph, C. Delivery of mRNA Therapeutics for the Treatment of Hepatic Diseases. *Mol. Ther.* **27**, 794–802 (2019).

64. Samaridou, E., Heyes, J. & Lutwyche, P. Lipid nanoparticles for nucleic acid delivery: Current perspectives. *Adv. Drug Deliv. Rev.* **154–155**, 37–63 (2020).

65.   Mout, R., Ray, M., Lee, Y. W., Scaletti, F. & Rotello, V. M. In Vivo Delivery of CRISPR/Cas9 for Therapeutic Gene Editing: Progress and Challenges. *Bioconjug. Chem.* **28**, 880–884 (2017).

66.   Zhang, N.-N. *et al.* A Thermostable mRNA Vaccine against COVID-19. *Cell* **182**, 1271–1283 (2020).

67.   Lu, J. *et al.* A COVID-19 mRNA vaccine encoding SARS-CoV-2 virus-like particles induces a strong antiviral-like immune response in mice. *Cell Res.* **30**, 936–939 (2020).